MATERIALS CHARACTERIZATION 81 (2013) 28–36

Available online at www.sciencedirect.com

SciVerse ScienceDirect

www.elsevier.com/locate/matchar

Synthesis and characterization of magnetite nanoparticles coated with lauric acid

J.B. Mamani[a,*], A.J. Costa-Filho[b], D.R. Cornejo[c], E.D. Vieira[d], L.F. Gamarra[a]

[a]Instituto do Cérebro-InCe, Hospital Israelita Albert Einstein-HIAE, 05651-901 São Paulo, Brazil
[b]Faculdade de Filosofia, Ciências e Letras de Ribeirão Preto, Universidade de São Paulo, Ribeirão Preto, Brazil
[c]Instituto de Física Universidade de São Paulo, USP, São Paulo, Brazil
[d]Instituto de Física, Universidade Federal de Goiás, Goiânia, Brazil

ARTICLE DATA

Article history:
Received 20 August 2012
Received in revised form
29 March 2013
Accepted 1 April 2013

Keywords:
Nanoparticles
Characterization
Synthesis
Magnetite
Lauric acid
Iron oxide

ABSTRACT

Understanding the process of synthesis of magnetic nanoparticles is important for its implementation in *in vitro* and *in vivo* studies. In this work we report the synthesis of magnetic nanoparticles made from ferrous oxide through coprecipitation chemical process. The nanostructured material was coated with lauric acid and dispersed in aqueous medium containing surfactant that yielded a stable colloidal suspension. The characterization of magnetic nanoparticles with distinct physico-chemical configurations is fundamental for biomedical applications. Therefore magnetic nanoparticles were characterized in terms of their morphology by means of TEM and DLS, which showed a polydispersed set of spherical nanoparticles (average diameter of ca. 9 nm) as a result of the protocol. The structural properties were characterized by using X-ray diffraction (XRD). XRD pattern showed the presence of peaks corresponding to the spinel phase of magnetite (Fe_3O_4). The relaxivities r_2 and r_2^* values were determined from the transverse relaxation times T_2 and T_2^* at 3 T. Magnetic characterization was performed using SQUID and FMR, which evidenced the superparamagnetic properties of the nanoparticles. Thermal characterization using DSC showed exothermic events associated with the oxidation of magnetite to maghemite.

1. Introduction

Great interest in the use of magnetic nanoparticles (MNPs) in areas such as bionanotechnology and biomedicine is mainly due to the diverse properties presented by this kind of material, related to its size and composition, when compared to the bulk material. Applications in these areas need MNPs that form stable colloidal suspensions, in addition to being compatible, non-toxic and non-immunogenic. Iron oxide MNPs are constituted by a magnetite (Fe_3O_4) or maghemite (γ-Fe_2O_3) core coated with biocompatible layers, usually made from polymers (proteins, lipids, or shorter organic chains), bound to the core *via* silanes. The synthesis of MNPs has been performed through methods such as sol–gel [1], co-precipitation [2], hydrothermal synthesis [3,4], thermal decomposition [5,6], microemulsion [7], and colloidal chemistry method [8]. The wet chemical routes to MNPs are simpler and more efficient with considerable control over composition, size, and even shape of the MNPs [9–11]. Among all these synthesis routes, the co-precipitation method has proved to be a method with potential for the synthesis of MNPs. One of the advantages of this technology is the capacity of mass production of MNPs properly functionalized. For biomedical applications the most widely used synthetic route is coprecipitation. This synthesis method is easy and inexpensive to prepare aqueous dispersions of MNPs because the synthesis is conducted in water. The coprecipitation

* *Corresponding author at: Instituto Israelita de Ensino e Pesquisa Albert Einstein (IIEPAE), Av.* Albert Einstein, 627/701, Piso Chinuch (2S), Morumbi, São Paulo/SP, CEP 05651-901, Brazil. Tel.: +55 11 21512044; fax: +55 11 3813 4334.
E-mail address: javierbm@einstein.br (J.B. Mamani).

1044-5803/$ – see front matter
http://dx.doi.org/10.1016/j.matchar.2013.04.001

method was chosen because of its potential for large-scale manufacturing, cost-effectiveness, easiness of production, and hydrophilicity of nanomaterials (important property for biomedical applications) [12]. In the coprecipitation method, iron oxide MNPs are synthesized *via* the coprecipitation of aqueous solutions containing Fe^{2+} and Fe^{3+} salts after the addition of a base [13]. The control of size, shape and composition depends on the salts used (chlorides, sulfates, nitrates, and so on), Fe^{2+} and Fe^{3+} ratio, pH, and ionic strength of the medium [14,15]. A convenient coat makes it possible to disperse the MNPs in adequate solvents.

Nanoparticle biocompatibility is determined by the coating material and the nucleus. The most frequent crystalline phase of iron oxide in biomedical applications is the magnetite, which can be obtained by the co-precipitation method; dextran is the coverage used in commercial NPMs for clinical applications due to its biocompatibility; however, the layer of dextran is lost by the enzymatic degradation during *in vivo* studies [16]. Depending on the applications several types of coatings can be used, such as: lauric acid (LA), poly(vinyl alcohol) (PVA), chitosan, poly(ethylene glycol) (PEG), starch, among others. LA is a fatty acid with a 12-carbon atom chain approved for pharmaceutical use and in the food industry, which produces a colloidal suspension of NPMs with a stable iron oxide base in the water. MNPs coated with LA present themselves as biocompatibles when used in low concentrations in *in vitro* applications [17].

Iron oxide based MNPs coated with LA are presented with potential in intracellular marking studies and monitoring by magnetic resonance imaging (MRI) [18]. However, effective internalization of MNPs in the cells is necessary for an effective detection by several techniques; to this end, previous knowledge of the characteristics of MNPs is required. The characterization of MNPs with distinct physico-chemical configurations is fundamental for biomedical applications. This requires specific studies, usually using several techniques, to determine and to exploit the properties of MNPs, which can then enhance its potential of use for new applications. Every colloidal system containing the MNPs interacts with external magnetic field, thus facilitating the medical diagnostic such as observed in MRI [18], where MNPs are used as contrast agents, or in cancer therapy known as magneto hyperthermia (MHT) that utilizes an AC magnetic field [19].

Understanding the synthesis and characterizing MNPs is a crucial step towards, for example, the implementation of intracellular labeling protocols of several cell lines [20] and/or for quantification processes in MRI [21] and in ferromagnetic resonance (FMR) [22] during *in vitro* and *in vivo* studies, which in turn contribute as an efficient tool in applications of MHT [19,23].

In this paper, we report on the synthesis of MNPs obtained *via* coprecipitation method coated by LA. We also present a detailed description of the various characterizations made from MNPs coated with LA, which is presented with applicability for intracellular marking and monitoring by the utilization as an agent of contrast in MRI, as well as with potential for the MHT technique. Transmission electron microscopy (TEM), dynamic light scattering (DLS), X-ray diffraction (XRD), magnetic measurements by SQUID magnetometer and ferromagnetic resonance (FMR), MRI, and calorimetric measurements by differential scanning calorimetry (DSC) were employed to characterize systematically the morphology, size, structure, magnetic property, relaxivity and calorimetric property of the MNPs coated by LA.

2. Materials and Methods

2.1. Synthesis of MNPs

The analytical grade reagents were commercially available and used without further purification protocols. Iron (III) chloride hexahydrate ($FeCl_3{\cdot}6H_2O$), iron (II) chloride tetrahydrate ($FeCl_2{\cdot}4H_2O$) and lauric acid (LA) ($CH_3(CH_2)_{10}COOH$) were purchased from Aldrich. Ammonium hydroxide (NH_4OH), hydrochloric acid (HCl), acetone ($CH_3(CO)CH_3$) and butyl alcohol (C_4H_9OH) were purchased from Sigma. Nonylphenol ethoxylated (*Renex-100®*) was obtained from Oxiteno.

A well-known procedure of coprecipitation of aqueous solutions containing mixtures of Fe^{2+} and Fe^{3+} was used to synthesize the iron oxide MNPs [24,25]. The synthesis followed the procedure carried out by Berger et al. [25]. Solutions of $FeCl_3{\cdot}6H_2O$ (0.1 M), $FeCl_2{\cdot}4H_2O$ (0.2 M) and HCl (1.5 M) were used in the preparations. In those solutions, we added 5% (v/v) of *Renex-100®* surfactant to control the formation of aggregates. The procedure was conducted in a reactor with N_2 atmosphere. In general terms, the synthesis is based on the precipitation of Fe_3O_4 after the addition of NH_4OH to the solutions containing salts of Fe^{2+} and Fe^{3+} in water until a pH value of 12 is reached. The chemical reaction is as follows [26]:

$$Fe^{2+} + 2Fe^{3+} + 8OH^- \Rightarrow Fe_3O_4 + 4H_2O.$$

The MNP precipitate was then washed five times with butyl alcohol. For the coating of the MNPs, a mass of LA to MPN ratio of 3/2 [27] was dissolved in deionized water, then heated to 333 K and kept under shaking until flocculation happens, which is the coated MNPs. MNPs coated with LA were then washed with acetone to remove the excess fatty acid. MNPs coated with LA were dispersed in aqueous medium containing *Renex-100®* surfactant that yielded a stable colloidal suspension.

2.2. Characterization of MNPs

2.2.1. Total Iron Concentration by ICP-AES

The elemental concentration of iron in the colloidal suspension of MNPs was determined using the inductively coupled plasma atomic emission spectroscopy (ICP-AES) technique that yielded the value: [Fe] = 3.06 ± 0.03 mg/mL.

2.2.2. Transmission Electron Microscopy (TEM)

The morphology of the MNPs in the colloidal suspension was observed with a Leo 906E (Zeiss) TEM microscope at 100 kV. A drop of the colloidal suspension (100 μg Fe/mL) was dispersed and dried on a copper grid covered with collodion and carbon prior to the experiment.

2.2.3. Dynamic Light Scattering (DLS)

The hydrodynamic size distribution and zeta potential measurements were performed with a Malvern Zetasizer Nano S. The number-weighted hydrodynamic distributions were determined

at an angle of 173° by Dynamic Light Scattering (DLS). These measurements were carried out at 296 K and, at least, in triplicate. The solution was filtered through Millipore nylon filters (pore size 0.45 μm) to eliminate dust and large contaminants. The size distribution analyses were determined by fitting the light scattering intensity autocorrelation function with CONTIN algorithm [28].

2.2.4. X-Ray Diffraction (XRD)

XRD experiments of the crystalline phase of a powder sample of non-coated MNPs were performed using an X-ray diffractometer (Rigaku D/max-γ, Japan) and Cu – K_α(λ = 1.5418 Å) radiation. The parameters of the measurements were: 40 kV and 30 mA, angular variation range 15 to 100° in steps of 0.05° for each 10 s (geometry θ – 2θ).

2.2.5. Magnetic Measurements by SQUID

Magnetic measurements were carried out with a Superconducting Quantum Interference Device magnetometer (SQUID) manufactured by Quantum Design Inc. The sample was a colloidal system (20 μL) composed of MNPs dispersed in water, which were mounted in a small quartz cylinder and sealed with photosensitive resin. Magnetization curves in conditions of zero-field-cooled (ZFC) and field-cooled (FC) were measured in the temperature range of 10–250 K in the presence of an applied field of 100 Oe. Hysteresis cycles for temperatures between 10 and 100 K were obtained with a maximum applied field of 20 KOe. The *ac* magnetic susceptibility as a function of temperature, with in-phase ($\chi'(T)$) and out-of-phase ($\chi''(T)$) components, was measured with null *dc* field and in the presence of an excitation magnetic field of 2 Oe and frequencies 0.71, 2.1, 7.1, 21.0, 71.1, 211.1 and 710.2 Hz.

2.2.6. Magnetic Measurements by FMR

FMR spectra were measured at 9.2 GHz using a Bruker ELEXSYS E580 spectrometer. The sample was positioned inside a TE_{102} rectangular cavity and the spectra of MNPs in a colloidal suspension (3.06 mg Fe/mL) were acquired at different temperatures (4–300 K). The temperature was controlled using an Oxford ITC-503 cryostat.

2.2.7. Relaxometric Measurements by MRI

The relaxometric characterization was performed using a clinical 3 T Siemens Symphony MRI unit (Trio, Siemens, Germany) equipped with a 32-channel brain coil. The protocols used for image acquisition were as described by Gamarra et al. [29]. The transverse relaxation times (T_2 and T_2^*) of MNPs were measured in colloidal suspensions with different concentrations (resistance 18.2 MΩ). The multi-contrast turbo-spin echo (SE_MC) sequence was used for measuring T_2 with the decay for each MNP sample being adjusted to a monoexponential behavior given by $\text{signal}_{SE\_MC} = S_0 \exp(-TE/T_2)$, where TE is the echo time and S_0 is the initial amplitude. The multi-echo gradient echo (GE) was used for measuring T_2^* with the signal intensities of IRM *vs* TEs being adjusted to $\text{signal}_{GE} = S_0 \exp(-TE/T_2^*)$.

2.2.8. Calorimetric Measurements by DSC

The thermal properties of non-coated MNPs were investigated by differential scanning calorimetry (DSC). To oxidize MNPs during the DSC measurements, a series of experiments was carried out with samples heated under a dynamic atmosphere of O_2 (20%) and N_2 (80%) at a rate of 1.0 L min^{-1}. Measurements of the heat flow in the temperature range of 663–853 K were recorded for (13.2 ± 0.1) mg of sample placed in aluminum pans and heated at a rate of 15 K/min. The DSC trace was measured using a NETZSCH DSC 200 *F3 Maia*® Instrument equipped with a SiC oven. The baseline was corrected by subtracting from the data the signal obtained from the empty aluminum pan. The software Netzsch Proteus was used for data analyses [30].

3. Results and Discussions

3.1. Transmission Electron Microscopy (TEM)

In Fig. 1, the TEM result shows the details of the poly-dispersity in size of the MNPs, which was analyzed from the TEM images by using the java version of the software ImageJ v 1.33u [31]. The average diameter was determined by adjusting the data to a log normal distribution given by: $f(D_p) = \frac{1}{\sqrt{2\pi}\omega_P D_p} \exp\left(-\frac{\left(\ln D_P - \ln D_P^0\right)^2}{2\omega_P^2}\right)$, where the average diameter is $< D_P > = D_P^0 \exp(\omega_P^2/2)$ and ω_P is the standard deviation around $\ln D_P^0$. The standard deviation of the mean diameter σ_P is $\sigma_P = D_P^0[\exp(2\omega_P^2) - \exp(\omega_P^2)]^{1/2}$. The analysis of the histograms shown on the inset in Fig. 1 (where we used more than 500 particles) resulted in an average diameter of $<D_P>$ = 9.4 nm and a standard deviation of σ_P = 3.0 nm.

3.2. Dynamic Light Scattering (DLS)

The DLS was employed to measure the size distribution of iron MNPs coated with LA in water solution. The number-weighted hydrodynamic diameter from light scattering intensity autocorrelation function is plotted in Fig. 2. The DLS results show a

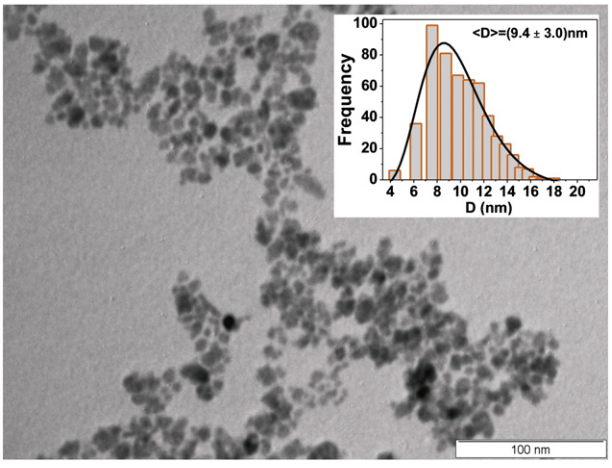

Fig. 1 – TEM image of MNPs. The number of particles used for the distribution was over 500. The inset shows the histogram of diameter distribution of the particles with average diameter and standard deviation of $<D_P>$ = 9.4 nm and σ_P = 3.0 nm, respectively.

polydispersed size distribution, which was fitted to a lognormal function and the mean hydrodynamic diameter outcome was D = (9.4 ± 2.3) nm. These results confirm the TEM analyses and demonstrate that the nanoparticles are well dispersed in solution.

3.3. *X-Ray Diffraction (XRD)*

Fig. 3 shows the result for the crystalline phase of non-coated MNPs obtained from XRD experiments. The peaks in the diffraction pattern correspond to an inverted spinel structure for the magnetite with a lattice parameter a_0 = 8.394 Å. The identification of the crystalline phase was performed by comparing our results with the PDF card (19-0629). The Debye–Scherrer formula [32] was used to obtain the average diameter from the most intense peak in Fig. 3 and yielded the value $D_{(hkl)}$ = (8.4 ± 0.4) nm.

3.4. *Magnetization and AC Susceptibility Behavior*

In Fig. 4a are shown the ZFC and FC curves for the ferrofluid. The sample was mounted in the SQUID at room temperature and then cooled down to 10 K without applied field. Immediately after cooling, a *dc* field of 100 Oe was applied and the temperature was increased slowly to 250 K: the magnetization was measured as a function of temperature, generating the ZFC curve (black-filled circles in Fig. 4a). The process continued with a new cooling down to 10 K, keeping the applied field, generating the FC curve (open circles in Fig. 4a). It can be seen in this figure that both curves are overlapping for temperatures above T_{irr} = (74 ± 2) K, which indicates that the system presents irreversibilities below that temperature and a superparamagnetic behavior above it. The maximum in the ZFC curve at T_B = (51 ± 2) K determines the average blocking temperature for the nanoparticles. The fact that T_{irr} value is greater than T_B is a consequence of the size distribution of nanoparticles in the ferrofluid and also of a possible distribution

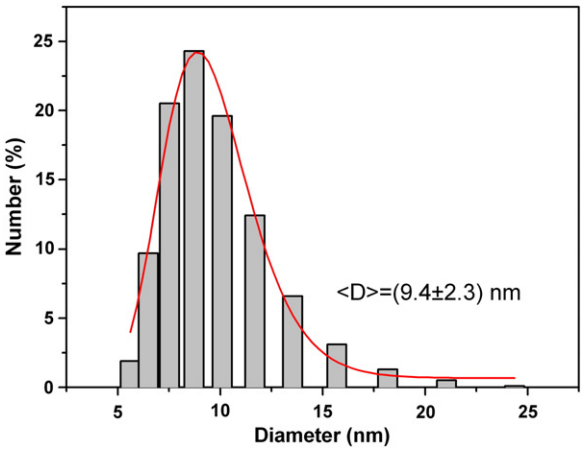

Fig. 2 – Size distribution by number of MNPs coated with LA dispersion. The DLS results show a polydispersed size distribution, the mean hydrodynamic diameter outcome was D = (9.4 ± 2.3) nm, assuming the log-normal size distribution.

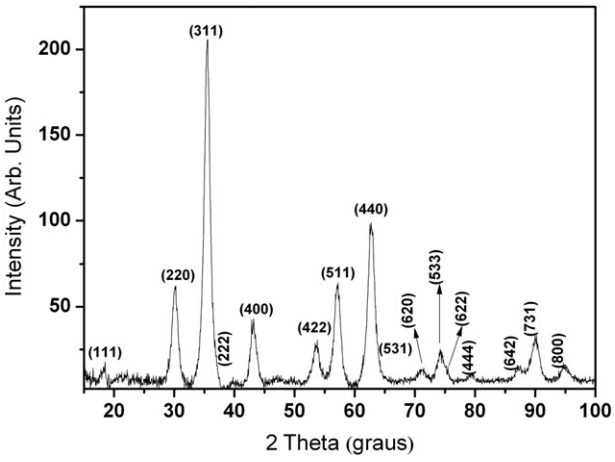

Fig. 3 – X-Ray diffraction pattern for non-coated MNPs. The peaks are representative of the crystalline phase of magnetite nanoparticles (PDF#19-0629).

of effective anisotropies in the particles. In fact, as can be seen in Fig. 2, a considerable fraction of particles with size greater than the average value is clearly present in the system. These

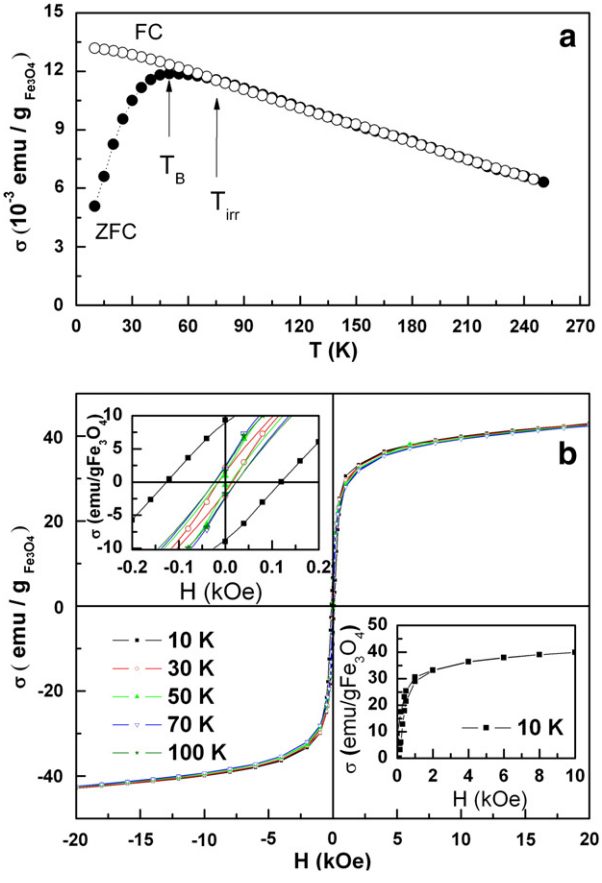

Fig. 4 – (a) Curves of ZFC (black-filled circles) and FC (open circles) magnetization for the sample of MNPs dispersed in water. (b) Hysteresis loops at temperatures 10, 30, 50, 70 and 100 K; insets in (b): details of the cycles in the field range −200 to 200 Oe (top left); details of the cycle at 10 K in high magnetic fields (lower right).

particles have higher energy barriers than the mean value (which is linked to T_B), and only reach the superparamagnetic state at temperatures T such that $T_{irr} > T > T_B$.

The hysteresis loops obtained at temperatures 10, 30, 50, 70 and 100 K are shown in Fig. 4b. The top inset in Fig. 4b shows some details of those curves at low values of the applied field. The irreversible behavior is evident for temperatures below T_B. For example, at T = 10 K the system presents a coercive field of 110 Oe. Upon raising the temperature, the magnetization curve gradually approaches a reversible-like curve (no hysteresis), compatible with a superparamagnetic behavior. However, even at 100 K the material has small remanence and coercivity (around 20 Oe), which show that there are still some blocked particles.

The reversible region of the hysteresis curves is achieved for applied fields of approximately 3 kOe (see the bottom right inset in Fig. 4b). This suggests that for those fields, all irreversible reversal of the magnetization has already occurred and only reversible rotations remain. The value 3 kOe can be used as an approximation for the anisotropy field of the system. From the hysteresis curve and extrapolating the data to infinite field, we can use the equation $M \cong M_S(1 - a/H - b/H^2)$ [33], where a and b are phenomenological parameters, to calculate the saturation magnetization M_S. Usually, a is interpreted as due to microstress and b as due to grain misalignment and the consequent changes in the effective anisotropy. Clearly these phenomena are present in a system of small particles, which has a high ratio surface/volume. Hence, at T = 10 K the value obtained was $\mu_0 M_S = 0.321(3)$ T, which is significantly lower than the corresponding value for the bulk ($\mu_0 M_S$ = 0.6 T), a fact clearly attributable to the nanometric size of the particles. Taking the anisotropy field value as 3 kOe (~240 kA/m), we can estimate a value for the effective anisotropy constant of the nanoparticles: $K_{eff} = \frac{1}{2} H_A \mu_0 M_S$, which yields $K_{eff} \cong 3.6 \times 10^4 J/m^3$. This value is three times greater than the corresponding value for the bulk material (1.2×10^4 J/m^3) [34].

The ratio between the remanence magnetization, $\mu_0 M_R$ = 0.06(1) T, and the saturation magnetization at 10 K is $R = M_R / M_S = 0.19$. This value is significantly lower than the theoretical value (R = 0.5) expected from the Stoner–Wohlfarth model for a set of randomly oriented non-interacting particles [33]. This value of R is thus an indication of the existence of demagnetizing interactions between the particles. A simple calculation considering the concentration and the average volume of the nanoparticles in the ferrofluid shows that the average distance between particles is of the order of 100 nm and the average magnetic moment of one particle is 3×10^{-20} Am^2. Hence, it is possible to estimate that a nanoparticle produces a magnetic field at 100 nm distance of approximately 2 A/m (ca. 160 Oe). The magnitude of this dipolar field is not negligible and might be the source of the demagnetizing interactions present in the system.

The components $\chi'(T)$ and $\chi''(T)$ of the magnetic susceptibility exhibit a maximum that depends on the frequency of the excitation field. It can be observed that, as expected, the maximum shifts towards higher temperatures with the increase of the frequency f. Such behavior is characteristic of a system of magnetic particles passing through the blocking temperature $T_B(f)$. It can be considered that, in the superparamagnetic regime, the relaxation time τ of the particle over its activation energy E_a, at a certain temperature T, follows the Néel–Arrhenius law [35]:

$$\tau = \tau_0 \exp\left(\frac{E_a}{k_B T}\right), \quad (1)$$

where τ_0 (average time between attempts to jump over the energy barrier) is of the order of 10^{-12}–10^{-9} s. Considering that $\tau = 1/f$ and that $T_B(f)$ corresponds to the maximum of the out-of-phase component $\chi''(T)$, we can build the curve $ln(\tau)$ *vs* $1/T_B$ as shown in Fig. 5. The linear dependence between $ln(\tau)$ and $1/T_B$ indicates that the reversal magnetization in the superparamagnetic regime is thermally activated. The fit of such curve to Eq. (1) yields $\tau_0 = 2.8(1) \times 10^{-10}$ s, which is a reasonable value for a system of particles in the superparamagnetic regime. From the same fit we can determine the activation energy $E_a = 1.17(4) \times 10^{-20}$ J. Taking into account that we can write such energy barrier as $E_a = K_{eff} V$, where V is the average volume of the nanoparticle, we obtain $K_{eff} = 4.0 \times 10^4$ J/m^3, which is once more much higher than the value corresponding to the bulk sample and roughly agrees with the estimate based on the magnetization curves. We do not expect significant contributions either from the shape anisotropy for quasi-spherical particles or from the exchange energy between particles (due to the dilution of the sample). The major source for the increase in anisotropy should come from the dipolar interactions. It is well known that dipolar interactions in systems of diluted nanoparticles (ferrofluids) can present notable magnitudes even at relatively low concentrations [36] and our estimate of the dipolar field agrees with such observation.

3.5. *Magnetic Measurements by FMR*

The FMR spectra (Fig. 6) show only one asymmetric resonance line whose peak-to-peak amplitude and resonance field shift in

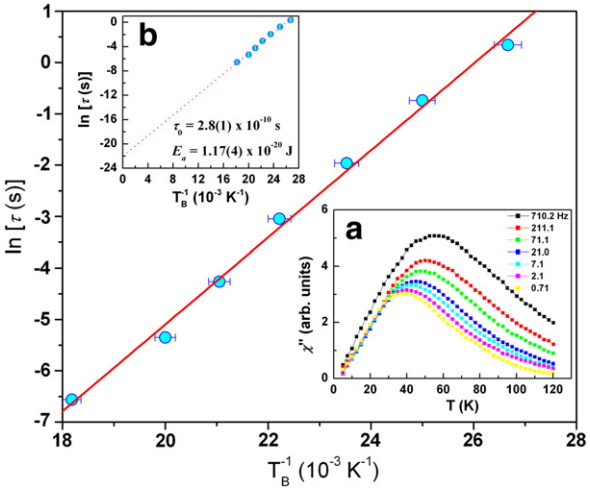

Fig. 5 – Arrhenius plot for the FA sample. T_B was determined from the maximum of the $\chi''(f,T)$ component of the *ac* magnetic susceptibility (panel a). The solid line represents the best fit of the experimental data to Eq. (1). In panel b, it is shown the extrapolation of that line to infinite temperature and also the parameters obtained from the fit.

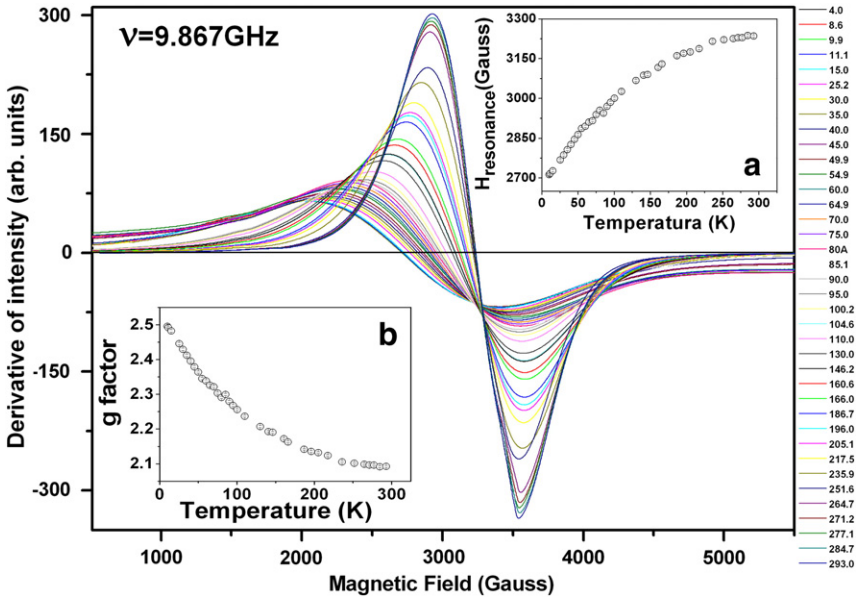

Fig. 6 – FMR spectra of MNPs in colloidal suspensions as a function of the temperature in the range 4–300 K. The insets show: (a) thermal variations in the $H_{resonance}$ values and (b) thermal variations in g-factor.

the measured temperature range. This is due to the temperature dependence of the FMR linewidth in spectra from randomly oriented ferromagnetic dispersion. At low temperatures, the linewidth is large due to the dispersion of the particles in the direction of the anisotropy field. Upon temperature increase, isotropic magnetic moments are formed, thus leading to the decrease of the linewidth. Fig. 6a shows the thermal variation of the resonance fields ($H_{resonance}$) obtained from the center of the spectra. The values of the g-factor were then calculated using: $g = (h\nu/(\beta H_0)) = (2.18 \pm 0.02)$ (at 300 K), where $\nu = 9.428$ GHz, h is the Planck's constant and β is the Bohr magneton. The g-factor at 300 K is in good agreement with the value g = 2.25 of spherical isolated magnetite MNPs, which presented spectrum with a 5000 Gauss linewidth and a typical superparamagnetic behavior [37]. In Fig. 6b it is shown the decrease in g-factor with the increase in temperature.

Fig. 7 shows the changes in the peak-to-peak linewidth (ΔH_{PP}) as the temperature is increased. The linewidth values decrease when going to higher temperatures, following the predictions for FMR spectra of superparamagnetic particles [38,39]. Thus, it is expected that the broadening and the shifts of the resonance signals be associated with the magnetization blocking of the MNPs. Moreover, the decrease in ΔH_{pp} within the measured temperature range is accompanied by an increase in $H_{resonance}$, showing an inverse behavior (Figs. 6a and 7), which is typical of synthetic nanoparticles [39].

According to Nagata and Ishihara [40,41], a superparamagnetic system of MNPs presents a simple power dependence between the shifts in the resonance fields ($\delta H_{resonance}$) and the linewidth of the spectra. The behavior of ln $\delta H_{resonance}$ *versus* ln ΔH_{pp} is shown on the inset in Fig. 7, where $\delta H_{resonance} = H_0 - H_{resonance}$ and H_0 corresponds to a g = (2.18 ± 0.10). The slope of the graph n = 3.2 ± 0.2 is consistent with a randomly oriented system. So, we conclude that the behavior of MNPs is superparamagnetic, isolated, and randomly oriented.

3.6. *Relaxometric Measurements by MRI*

The proton relaxation times T_2 and T_2^* were obtained from MRI experiments using a phantom made of cavities containing colloidal suspensions of MNPs in agarose (1% w/w) and with iron concentrations of 1.5, 4.5, 7.5, 10.5, 15, 19.5, 24, 30, 34.5, 37.5, 40.5, 45, 49.5, 54 and 60 μg Fe/mL (Fig. 8a). Fig. 8 presents the linear dependence of the relaxation rates $1/T_2$ and $1/T_2^*$ on the iron concentration ([Fe]).

The images obtained by using the sequences SE_MC (Fig. 8a) and GE (Fig. 8b) at different MNP concentrations show the decrease in the signal intensity when the concentration is increased due to the shortening of T_2 and T_2^*. The relaxation rates ($1/T_2$ and $1/T_2^*$) (in ms^{-1}) are correlated to the MNP concentration in solution and to their relaxivities r_2 and r_2^* (in ms^{-1} mL/μg), relaxivities (r_1, r_2 and r_2^*) is a property of the

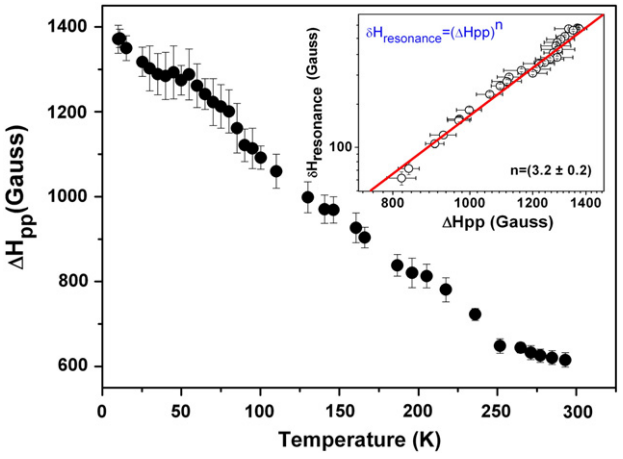

Fig. 7 – Thermal variation of ΔH_{PP} obtained from the FMR spectra. The inset shows the dependence between $\delta H_{resonance}$ and ΔH_{PP} with a value of n = 3.2 ± 0.2.

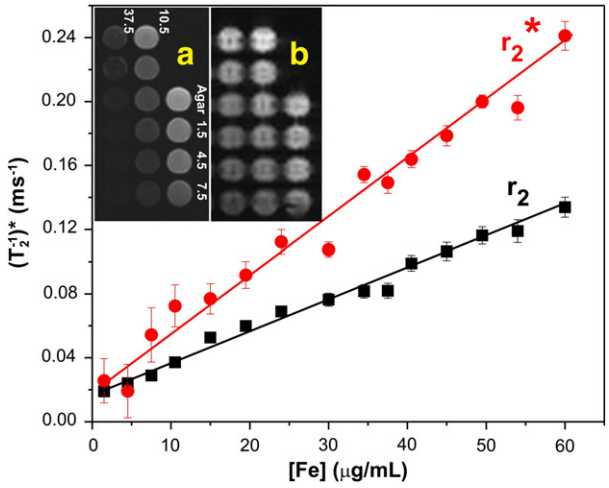

Fig. 8 – Dependence of the relaxations rates $1/T_2$ and $1/T_2^*$ on the iron concentration [Fe]. (a) Weighted images in T_2 obtained using the sequence SE_MC on the phantom with TR = 1700 ms and TE = 24 ms. Some values of [Fe] are indicated in the image; (b) weighted images in T_2^* obtained using the sequence GE on the phantom with TR = 83 ms and TE = 5.63 ms.

nanoparticle material that depends on the size and varies according to the magnetic field [42]. The rate $1/T_2$, also valid for $1/T_2^*$, can be expressed as [43]:

$$\frac{1}{T_2^{\text{Sample}}} = \left(\frac{1}{T_2^{\text{Suspension}}}\right)_{[\text{Fe}]=0} + [\text{Fe}] \times r_2. \quad (2)$$

The relaxivities r_2 and r_2^*, in ms^{-1} mL/μg, were determined from the slopes of a least-squares linear fit of the experimental data in Fig. 8 and yielded the values: $r_2 = (20.2 \pm 0.4) \times 10^{-4}$ ms^{-1} μg^{-1} mL and $r_2^* = (35.8 \pm 1.3) \times 10^{-4}$ ms^{-1} μg^{-1} mL.

In MRI, the relaxation times can be experimentally manipulated by using contrast agents. For example, T_1 can be altered by the use of gadolinium or manganese, and T_2 by the presence of particulate iron oxide since T_2 is more influenced by magnetic inhomogeneities. The decrease in T_2^* due to the presence of MNPs produces local inhomogeneities in the applied magnetic field that, in turn, promotes dephasing and altering the relaxation time T_2^*. To achieve the maximum effect of the contrast agent in T_2, the ferrites should be coated with thin layers, if possible, since the interaction between magnetic particles and water molecules depends on their interdistance. Then, the quantification of the MNPs uptaken in tissues, captured by cells or in water suspensions has to be weighted in the relaxation times T_2 and T_2^*. For instance, the iron ($[\text{Fe}]_{\text{uptake}}$) uptaken in incubated cells submitted to a certain amount of iron can be determined by means of the following equation:

$$[\text{Fe}]_{\text{uptake}} = \frac{(1/T_2)^{\text{Labeled cell}} - (1/T_2)^{\text{Not labeled cell}}}{r_2} \quad (3)$$

where r_2 is the relaxitivity (determined in a previous assay), $1/T_2^{\text{Not labeled cell}}$ is the relaxation rate of non-labeled cells, and $1/T_2^{\text{Labeled cell}}$ the relaxation rate in labeled cells.

3.7. Calorimetric Measurements by DSC

Thermal analysis of the Fe_3O_4 sample synthesized is presented in Fig. 9. The DSC trace presents an exothermic event at around 756 K for a heating rate of 15 K/min, related to the oxidation of Fe_3O_4 to $\gamma - Fe_2O_3$. The exothermic event was attributed to oxygen diffusion in the core of the particles and complete transformation to maghemite phase, as indicated in the following equation:

$$2Fe_3O_4 + O_2 \rightarrow 3\gamma Fe_2O_3. \quad (4)$$

In this reaction, O_2 is required to complete the reaction [44]. This is supported by the depletion of O_2 during the transition from the crystalline phase to iron oxide.

3.8. Perspectives for the Applicability of NPMs Coated with LA

The size of the MNPs coated with LA determined by the XRD, TEM and DLS techniques presents themselves as appropriate for the interaction and adhesion with cells due to the fact that MNPs smaller than 50 nm cross the physiological barriers by the paracellular passage mechanism [45], being that, generally, MNPs with a hydrodynamic diameter from 10 nm to 100 nm are pharmacokinetically optimal for *in vivo* applications.

Iron oxide based MNPs coated with different materials influence the modulation of biocompatibility and interaction with the cells [46]. Pradhan et al. carried out qualitative and quantitative studies of cellular internalization with MNPs of magnetite coated with dextran and LA [17]. The study showed that MNPs coated with LA exhibit cytocompatibility less than or equal to MNPs coated with dextran at concentrations less than 100 μg Fe/ml used for the incubation of *HeLa* and *L929* cells, as well as an efficient cellular uptake of MNPs that could be subjected to the cellular interactions with the nature of the surface coverage related to adhesion, internalization and intracellular destination [47].

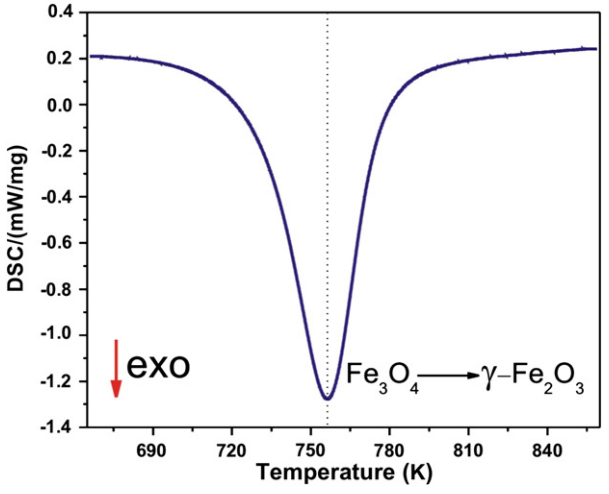

Fig. 9 – DSC analysis of synthesized particles. Trace obtained at heating rate of 15 K/min for the oxidation of Fe_3O_4 in 20% O_2 and 80% N_2.

Several contrast agents used in MRI based on iron oxide based MNPs as ferumoxides, which are MNPs coated with dextran, are used in the clinic in MRI. However, MNPs covered with dextran do not show good cellular uptake for effective monitoring of non-phagocytic cells [48]. This can be solved using transfection agents such as poly-L-lysine (PLL) [48,49] and protamine sulfate [50], but PLL is not accepted for biomedical applications because of its toxicity at high concentrations [51]. Nonetheless, MNPs coated with LA show that they are taken in an efficient way, without the need of transfection agents, by the monitoring cells. All this is associated to the physico-chemical characteristics and the interaction of LA, coating material, with the cells [17]. Due to their high magnetic susceptibility, MNPs coated with LA can be used as a negative contrast agent in the MRI technique, as well as for the visualization in high resolution cell's homing after being labeled for concentrations less than 100 μg Fe/ml.

In the MHT technique, particles with high hysteresis are desirable due to the fact that they release more heat with a lower dose of nanoparticles administered to the tumorigenic tissue [16,19,23]. Iron oxide based MNPs are ideal for applications in MHT because iron presents a high value of magnetic saturation (220 emu/g). Therefore, NPMs coated with LA have an application potential in this technique, in addition to fulfilling the requirements needed for the *in vivo* studies such as biocompatibility, non-toxic at low concentrations, good uptake by the cells and good dispersion in aqueous solution [17].

4. Conclusions

The coprecipitation method was used to synthesize MNPs coated with lauric acid and dispersed in water at an iron concentration of [Fe] = 3.06 ± 0.03 mg/mL. The morphological characterization by means of TEM and DSL showed polydispersed spherical particles with and average diameter of $< D_P > = (9.4 \pm 3.0)$ nm and $< D > = (9.38 \pm 2.30)$ nm, respectively. The structural characterization using XRD determined a crystalline phase with size $D_{(hkl)} = (8.4 \pm 0.4)$ nm as estimated from the Debye–Scherrer relation. From the values of the transversal relaxation times T_2 and T_2^* we determined the relaxitivities $r_2 = (20.2 \pm 0.4) \times 10^{-4}\ ms^{-1}\ \mu g^{-1}\ mL$ and $r_2^* = (35.8 \pm 1.3) \times 10^{-4}\ ms^{-1}\ \mu g^{-1}$ mL at 3 T. These two parameters are fundamental for the quantification of iron uptake by cells. The magnetic characterization *via* SQUID and FMR led to: (i) SQUID: the ZFC and FC magnetization experiments showed a blockage temperature of 51 K. For $T > T_B$ the hysteresis cycle did not exhibit coercivity due to the superparamagnetic behavior of the MNPs. For $T < T_B$, the coercive field present in the hysteresis cycle indicated the transition from the superparamagnetic to a ferromagnetic state. $\chi'(T)$ and $\chi''(T)$ exhibited the expected behavior for a superparamagnetic system. The correlation time $\tau_0 = (2.8 \pm 0.1) \times 10^{-10}$s is also consistent with a superparamagnetic system. Contributions to the activation energy $E_a = (1.17 \pm 0.04) \times 10^{-20}$J may come from intrinsic anisotropy and interparticle interactions. (ii) FMR: The samples analyzed in the temperature range 4–300 K evidenced a superparamagnetic state below T_B. Thermal analysis revealed a phase transition from the magnetite to γ-phase at around 756 K.

Acknowledgments

This work was supported by the Instituto Israelita de Ensino e Pesquisa Albert Einstein and the Brazilian agencies FINEP, CAPES, CNPq, and FAPESP.

REFERENCES

[1] Sagrario MM, Gracia-Cerda LA, Lubian TJR. Preparation and characterization of cobalt ferrite by the polymerized complex method. Mater Lett 2005;59:1056–60.
[2] Galindo BR, Valenzuela AO, Gracia-Cerda LA, Fernandez RO, Aquino MJ, Ramos G, et al. Synthesis and magneto-structural study of $Co_xFe_{3-x}O_4$ nanoparticles. J Magn Magn Mater 2005;294:e33–6.
[3] Sreeja V, Joy PA. Microwave-hydrothermal synthesis of γ-Fe_2O_3 nanoparticles and their magnetic properties. Mater Res Bull 2007;42(8):1570–6.
[4] Daou TJ, Pourroy G, Begin-Colin S, Greneche JM, Ulhaq-Bouillet C, Legare P, et al. Hydrothermal synthesis of monodisperse magnetite nanoparticles. Chem Mater 2006;18(18):4399–404.
[5] Simeonidis K, Mourdikoudis S, Moulla M, Tsiaoussis I, Martinez-Boubeta C, Angelakeris M, et al. Controlled synthesis and phase characterization of Fe-based nanoparticles obtained by thermal decomposition. J Magn Magn Mater 2007;316(2):e1–4.
[6] Zhou W, Tang K, Zeng S, Qi Y. Room temperature synthesis of rod-like $FeC_2O_4{\cdot}2H_2O$ and its transition to maghemite, magnetite and hematite nanorods through controlled thermal decomposition. Nanotechnology 2008;19(6):065602.
[7] Liu ZL, Wang X, Yao KL, Du GH, Lu QH, Ding ZH, et al. Synthesis of magnetite nanoparticles in W/O microemulsion. J Mater Sci 2004;39:2633.
[8] Cozzoli PD, Snoeck E, Garcia MA, Giannini C, Guagliardi A, Cervellino A, et al. Colloidal synthesis and characterization of tetrapod-shaped magnetic nanocrystals. Nano Lett 2006;6(9):1966–72.
[9] Gupta AK, Wells S. Surface-modified superparamagnetic nanoparticles for drug delivery: preparation, characterization, and cytotoxicity studies. IEEE Trans Nanobioscience 2004;3(1):66–73.
[10] Charles SW. Magnetic properties of fine particles. North-Holland: Elsevier; 1992267–374.
[11] Gupta AK, Curtis ASG. Lactoferrin and ceruloplasmin derivatized superparamagnetic iron oxide nanoparticles for targeting cell surface receptors. Biomaterials 2004;25(15):3029–40.
[12] Massart R, Cabuil V. Synthèse en milieu alcalin de magnétite colloïdale: contrôle du rendement et de la taille des particules. J Chim Phys 1987;84:961–73.
[13] Reimers GW, Khalafalla SE. Preparing magnetic fluids by a peptizing method. Washington: US Dept of the Interior, Bureau of Mines; 1972.
[14] Hadjipanayis GC, Siegel RW. Nanophase materials: synthesis, properties and applications. NATO ASI series, applied sciences, 260. Dordrecht: Kluwer; 1993.
[15] Sjogren CE, Briley-Saebo K, Hanson M, Johansson C. Magnetic characterization of iron oxides for magnetic resonance imaging. Magn Reson Med 1994;31(3):268–72.
[16] Jordan A, Wust P, Scholz R, Tesche B, Fahling H, Mitrovics T, et al. Cellular uptake of magnetic fluid particles and their

effects on human adenocarcinoma cells exposed to AC magnetic fields *in vitro*. Int J Hyperthermia 1996;12(6):705–22.
[17] Pradhan P, Giri J, Banerjee R, Bellare J, Bahadur D. Cellular interactions of lauric acid and dextran-coated magnetite nanoparticles. J Magn Magn Mater 2007;311(1):282–7.
[18] Kim EH, Lee HS, Kwak BK, Kim B. Synthesis of ferrofluid with magnetic nanoparticles by sonochemical method for MRI contrast agent. J Magn Magn Mater 2005;289:328–30.
[19] Jordan A, Scholz R, Wust P, Fahling H, Felix R. Magnetic fluid hyperthermia (MFH): cancer treatment with AC magnetic field induced excitation of biocompatible superparamagnetic nanoparticles. J Magn Magn Mater 1999;201:413–9.
[20] Conner SD, Schmid SL. Regulated portals of entry into the cell. Nature 2003;422:37–44.
[21] Liu W, Frank JA. Detection and quantification of magnetically labeled cells by cellular MRI. Eur J Radiol 2009;70:258–64.
[22] Gamarra LF, Costa-Filho AJ, Mamani JB, Ruiz RC, Pavon LF, Sibov TT, et al. Ferromagnetic resonance for the quantification of superparamagnetic iron oxide nanoparticles in biological materials. Int J Nanomedicine 2010;5:203–11.
[23] Thiesen B, Jordan A. Clinical applications of magnetic nanoparticles for hyperthermia. Int J Hyperthermia 2008;24(6):467–74.
[24] Lopez-Perez JA, Lopez-Quintela MA, Mira J, Rivas J. Preparation of magnetic fluids with particles obtained in microemulsions. IEEE Trans Magn 1997;33:4359–62.
[25] Berger P, Adelman NB, Beckman KJ, Campell DJ, Ellis AB, Lisensky GC. Preparation and properties of an aqueous ferrofluid. J Chem Educ 1999;76:943–8.
[26] Gupta AK, Gupta M. Synthesis and surface engineering of iron oxide nanoparticles for biomedical applications. Biomaterials 2005;26(18):3995–4021.
[27] Fu L, Dravid VP, Johnson DL. Self-assembled (SA) bilayer molecular coating on magnetic nanoparticles. Appl Surf Sci 2001;181:173–8.
[28] Lei-Shou Y, Guan-Ling Y, Zhen-Jiang H, Yi-Fang L. Iterative CONTIN algorithm for particle sizing in dynamic light scattering [J]. Opto-electronic engineering, 08. Guangzhou 510006, China: School of Physics and Telecommunication Engineering, South China Normal University; 2006.
[29] Gamarra LF, Amaro Jr E, Alves S, Soga D, Pontuschka WM, Mamani JB, et al. Characterization of the biocompatible magnetic colloid on the basis of Fe_3O_4 nanoparticles coated with dextran, used as contrast agent in magnetic resonance imaging. J Nanosci Nanotechnol 2010;10(7):4145–53.
[30] Opfermann J. Kinetic analysis using multivariate non-linear regression. J Therm Anal Calorim 2000;60:641–58.
[31] Rasvand W. Image processing and analysis in Java. [Internet] URL [updated 2003 January 21; cited 2012 July 12]. Available from http://rsb.info.nig.gov/ij.
[32] Kim DK, Zhang Y, Kehr J, Klason T, Bjelke B, Muhammed M. Characterization and MRI study of surfactant-coated superparamagnetic nanoparticles administered into the rat brain. J Magn Magn Mater 2001;225:256–61.
[33] Cullity BD, Graham CD. Introduction to magnetic materials. 2nd ed.New Jersey: John Wiley & Sons Inc.; 2009.
[34] McCurrie RA. Ferromagnetic materials, structure and properties. London: Academic Press; 1994.
[35] Guimarães AP. Principles of nanomagnetism. Springer; 2009.
[36] Luo W, Nagel SR, Rosenbaum TF, Rosensweig RE. Dipole interactions with random anisotropy in a frozen ferrofluid. Phys Rev Lett 1991;67:2721–4.
[37] Griscom DL. Ferromagnetic resonance of precipitated phases in natural glasses. J Non-Cryst Solids 1984;67:81–118.
[38] Tronconi AL, Moris PC, Pelegrini F, Tourinho FA. Electron paramagnetic resonance study of ionic water-based manganese ferrite ferrofluids. J Magn Magn Mater 1993;122:90–2.
[39] Kinnari P, Upadhyay RV, Mehta RV. Magnetic properties of Fe–Zn ferrite substituted ferrofluids. J Magn Magn Mater 2002;252:35–8.
[40] Nagata K, Ishihara A. ESR of ultrafine magnetic particles. J Magn Magn Mater 1992;104–107:1571–3.
[41] Wu KH, Chang YC, Chen HB, Yang CC, Horng DN. Variable temperature electron paramagnetic resonance studies of the NiZn ferrite/SiO_2 nanocomposite. J Magn Magn Mater 2004;278:156–63.
[42] Na HB, Song ICh, Hyeon T. Inorganic nanoparticles for MRI contrast agents. Adv Mater 2009;21:2133–48.
[43] Boutry S, Forge D, Burtea C, Mahieu I, Murariu O, Laurent S, et al. How to quantify iron in an aqueous or biological matrix: a technical note. Contrast Media Mol Imaging 2009;4:299–304.
[44] Sanders JP, Gallagher PK. Thermomagnetometric evidence of γ-Fe_2O_3 as an intermediate in the oxidation of magnetite. Thermochim Acta 2003;406:241–3.
[45] Florence AT, Hillery AM, Hussain N, Jani PU. Nanoparticles as carriers for oral peptide absorption: studies on particle uptake and fate. J Control Release 1995;36:39–46.
[46] Markides H, Rotherham M, El Haj AJ. Biocompatibility and toxicity of magnetic nanoparticles in regenerative medicine. J Nanomater 2012, http://dx.doi.org/10.1155/2012/614094.
[47] Berry CC, Wells S, Charles S, Curtis ASG. Dextran and albumin derivatised iron oxide nanoparticles: influence on fibroblasts *in vitro*. Biomaterials 2003;24:4551–7.
[48] Babic M, Horak D, Trchova M, Jendelova P, Glogarova K, Lesny P, et al. Poly(L-lysine)-modified iron oxide nanoparticles for stem cell labeling. Bioconjug Chem 2008;19:740–50.
[49] Arbab AS, Bashaw LA, Miller BR, Jordan EK, Bulte JW, Frank JA. Intracytoplasmic tagging of cells with ferumoxides and transfection agent for cellular magnetic resonance imaging after cell transplantation: methods and techniques. Transplantation 2003;76:1123–30.
[50] van Buul GM, Farrell E, Kops N, van Tiel ST, Bos PK, Weinans H, et al. Ferumoxides–protamine sulfate is more effective than ferucarbotran for cell labeling: implications for clinically applicable cell tracking using MRI. Contrast Media Mol Imaging 2009;4:230–6.
[51] Hongxu L, Likun G, Naoki K, Tetsuya T, Guoping Ch. Effects of poly(L-lysine), poly(acrylic acid) and poly(ethylene glycol) on the adhesion, proliferation and chondrogenic differentiation of human mesenchymal stem cells. J Biomater Sci Polym Ed 2009;20(5–6):577–89.